AIAA SciTech Forum
8–12 January 2018, Kissimmee, Florida
2018 AIAA Aerospace Sciences Meeting

10.2514/6.2018-0314



# Improved Delayed Detached Eddy Simulation of Super-Lift Flow of Co-Flow Jet Airfoil

Yunchao Yang* Michael Fernandez† Gecheng Zha‡
Dept. of Mechanical and Aerospace Engineering
University of Miami, Coral Gables, Florida 33124
E-mail: gzha@miami.edu

**Abstract**

This paper present the improved delayed detached eddy simulation (IDDES) of Co-Flow Jet (CFJ) flow control airfoil, with super lift coefficient that exceeds theoretical lift coefficient limit[1]. The spatially filtered Navier-Stokes equations are solved using a fifth-order WENO reconstruction scheme for the inviscid fluxes and a fourth order central differencing scheme for the viscous fluxes. The IDDES is developed based on the Spalart-Allmaras (S-A) turbulence model and it incorporates the wall modeled large eddy simulation (WMLES) capacity. The simulated wing span is 0.1 chord with periodic boundary condition applied in the spanwise direction. The IDDES simulation of the CFJ wing is carried out at the AoA of 62° with three different jet momentum coefficients $C_\mu$ of 0.25, 0.35 and 0.5. The super-lift coefficient of 9.1 is achieved at AoA = 62° and $C_\mu = 0.5$. The baseline NACA6421 wing is also simulated at AoA = 18° and the results show excellent agreement with the experiment. The comparison of the flow field of CFJ-NACA6421 and baseline NACA6421 airfoil shows that the CFJ can remove the flow separation at a high angle of attack. The high momentum jet provides adequate jet momentum to active the boundary layer and maintains the flow attached.The qualitative counter-rotating vortex structures at very high AoA and severe adverse pressure gradient is similar to those observed in 2D RANS simulation.



## Nomenclature

| | |
|---|---|
| $ESTOL$ | Extreme Short Take-Off and Landing |
| $AoA$ | Angle of Attack |
| $AFC$ | Active Flow Control |
| $CFJ$ | Co-Flow Jet |
| $FASIP$ | Flow-Acoustics-Structure Interaction Package |
| $LE$ | Leading Edge |
| $TE$ | Trailing Edge |
| $RANS$ | Reynolds-Averaged Navier-Stokes |
| $ZNMF$ | Zero-Net Mass Flux |
| $P$ | CFJ pumping power consumption, $P = \frac{\dot{m}C_pT_{t2}}{\eta}(\Gamma^{\frac{\gamma-1}{\gamma}} - 1)$ |
| $\eta$ | CFJ pumping system efficiency, propeller efficiency |
| $P_c$ | Power coefficient, $P_c = \frac{P}{\frac{1}{2}\rho_\infty V_\infty^3 S}$ |
| $PR$ | Total pressure ratio, $\Gamma$ |

* Ph.D. Candidate, AIAA student member
† Undergraduate student, AIAA student member
‡ Professor, ASME Fellow, AIAA associate Fellow

| | |
|---|---|
| $C_L$ | Lift coefficient |
| $C_D$ | Drag coefficient |
| $C_M$ | Moment coefficient |
| $C_\mu$ | Jet momentum coefficient, $C_\mu = \frac{\dot{m}V_j}{\frac{1}{2}\rho_\infty {V_\infty}^2 S}$ |
| $C_{Lmax}$ | Maximum lift coefficient |
| $(L/D)_c$ | Aerodynamic efficiency corrected for CFJ airfoil, $\frac{L}{D+P/V_\infty}$ |
| $C_L^2/C_D$ | Productivity efficiency coefficient |
| $(C_L^2/C_D)_c$ | Productivity efficiency coefficient corrected for CFJ airfoil, $(C_L^2/C_D)_c = C_L^2/(C_D + P_c)$ |
| $Re$ | Reynolds number |
| $Ma$ | Mach number |
| $M_{is}$ | Isentropic Mach number |
| $C_p$ | Pressure coefficient |
| $c_p$ | Constant pressure specific heat |
| $\gamma$ | Air specific heats ratio |
| $S$ | Platform area of the wing |
| $\rho_\infty$ | Freestream density |
| $V_\infty$ | Freestream velocity |
| $T_t$ | Total temperature |
| $P_t$ | Total pressure |
| $H_t$ | Total specific enthalpy |
| $\alpha$ | Angle of attack |
| $\dot{m}$ | Mass flow across the pump |
| $C$ | Chord length |
| $_j$ | Subscript, stands for jet |
| $_c$ | Subscript, stands for corrected |



# 1 Introduction

Wimpress, the Chief of Aerodynamics in Boeing Company, mentioned in 1968, achieving adequate low-speed aerodynamic characteristics for takeoff and landing of modern, high-performance airplanes is one of the most challenging goals of subsonic aerodynamic technology [2]. The Co-Flow Jet (CFJ) flow control technique developed by Zha and his group [3, 4, 5, 6, 7, 8, 9, 10, 11, 12] is one of the most promising technologies to achieve the extremely short take-off and landing performances (ESTOL). The concept of CFJ flow control airfoil is proposed by Zha et al. . The CFJ technique is able to achieve a dramatically lift augmentation, drag reduction and stall margin increase at a low energy consumption. It can not only achieve ESTOL performance with ultra-high lift coefficient but also significantly enhance cruise efficiency and cruise lift coefficient (wing loading) from subsonic to transonic conditions [10, 11, 12]. The CFJ airfoil has great potential to radically change the overall aircraft design philosophy from subsonic to transonic speeds.

The maximum lift coefficient $C_{Lmax}$ of an airfoil is critical to determine the aircraft take-off/landing distance. The super-lift coefficient $C_{Lmax} > 2\pi(1 + \frac{t}{c})$ is demonstrated by CFD simulation by the CFJ-NACA6421 airfoil in the previous research [1], which makes the CFJ flow control very promising to achieve the two goals of ultra-high cruise efficiency and extremely short take-off and landing .

The CFJ airfoil has an injection slot near the leading edge (LE) and a suction slot near the trailing edge (TE)

on the airfoil upper surface as sketched in Fig. 1. A small amount of mass flow is withdrawn into the airfoil near the TE, pressurized and energized by a pumping system inside the airfoil, and then injected near the LE in the direction tangent to the main flow. The CFJ flow control is a zero-net mass-flux flow control method since its whole CFJ system does not require any additional mass flow from other sources.

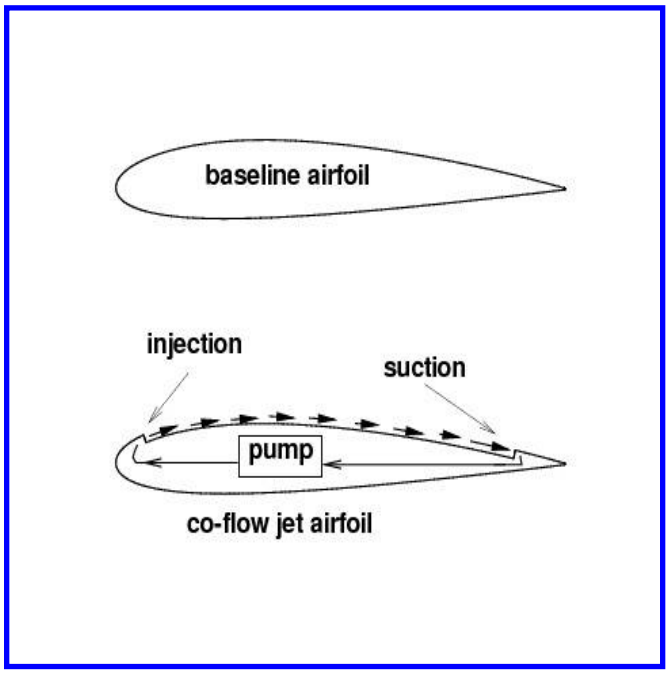


Figure 1: Baseline airfoil and CFJ airfoil.

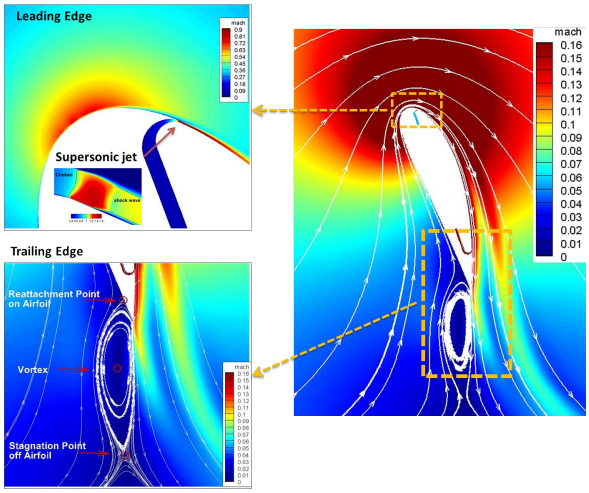


Figure 2: Mach number contours and streamlines at $C_\mu = 0.35$ and AoA =70° for the CFJ6421-SST016-SUC053-INJ009 airfoil.

Fig. 2 is the super-lift coefficient flow structures of the flow field obtained by CFD RANS simulation in [1]. A very high circulation detaches the stagnation point from the airfoil. The trailing edge vortex creates an extended virtual body to form a high-pressure region due to the stagnant flow to support the airfoil with a super-lift coefficient. The turbulent mixing and entrainment between the jet and main flow, energize the wall boundary-layer. It dramatically increases the circulation, augmenting lift, and reducing the total drag (or generates thrust) by filling the wake velocity deficit. The CFJ airfoil has a unique low energy expenditure mechanism because the jet gets injected at the leading edge suction peak location, where the main flow pressure is the lowest and makes it easy to eject the flow, and it gets sucked at near the trailing edge, where the main flow pressure is the highest and makes it easy to withdraw the flow.

Though two-dimensional Reynolds-averaged Navier-Strokes (RANS) simulation reveals the steady state large flow structures, the three-dimensional turbulent vortex flow structures and turbulent mixing process can not be well resolved by the RANS simulation due to its assumption of universal scale filtering. As an alternative, large eddy simulation (LES) is a more accurate approach to resolve the large turbulent flow structures and shear layer and reveal the flow mixing mechanisms. LES directly simulates the large eddies and models the small eddies that are more isotropic. However, LES requires very expensive computational resources. The hybrid RANS/LES approach is a promising compromise for engineering applications by taking the advantages of RANS's high efficiency within the wall boundary layers and LES's high accuracy with large flow structures outside of boundary layers [13]. Therefore, the improved delayed detached eddy simulation (IDDES) is employed in this study to investigate the baseline and super-lift CFJ flows at high angle of attacks.

The objective of this paper is two folds: 1) to demonstrate the maximum lift coefficient capability of the CFJ

airfoil using IDDES. 2) To investigate the vortical flow structures of the CFJ airfoil that sustains extremely severe adverse pressure gradient at high AoAs to obtain super-lift coefficient.

# 2 Numerical Methodology

## 2.1 Governing Equations

The spatially filtered Navier-Stokes governing equations in generalized coordinates are expressed as:

$$\frac{\partial \mathbf{Q}}{\partial t}+\frac{\partial \mathbf{E}}{\partial \xi}+\frac{\partial \mathbf{F}}{\partial \eta}+\frac{\partial \mathbf{G}}{\partial \zeta}=\frac{1}{Re}\left(\frac{\partial \mathbf{E}_v}{\partial \xi}+\frac{\partial \mathbf{F}_v}{\partial \eta}+\frac{\partial \mathbf{G}_v}{\partial \zeta}+\mathbf{S}\right) \tag{1}$$

where $Re$ is the Reynolds number. The equations are nondimenisonalized based on airfoil chord $L_\infty$, freestream density $\rho_\infty$ and velocity $U_\infty$.

The conservative variable vector $\mathbf{Q}$, the inviscid flux vectors $\mathbf{E}$, $\mathbf{F}$, $\mathbf{G}$, the viscous flux $\mathbf{E_v}$, $\mathbf{F_v}$, $\mathbf{G_v}$ and the source term vector $\mathbf{S}$ are expressed as

$$\mathbf{Q}=\frac{1}{J}\begin{pmatrix}\bar{\rho}\\ \bar{\rho}\tilde{u}\\ \bar{\rho}\tilde{v}\\ \bar{\rho}\tilde{w}\\ \bar{\rho}\tilde{e}\\ \bar{\rho}\tilde{\nu}_t\end{pmatrix},\mathbf{E}=\begin{pmatrix}\bar{\rho}U\\ \bar{\rho}\tilde{u}U+l_x\bar{p}\\ \bar{\rho}\tilde{v}U+l_y\bar{p}\\ \bar{\rho}\tilde{w}U+l_z\bar{p}\\ \left(\bar{\rho}\tilde{e}+\bar{p}\right)U-l_t\bar{p}\\ \bar{\rho}\tilde{\nu}U\end{pmatrix},\mathbf{F}=\begin{pmatrix}\bar{\rho}V\\ \bar{\rho}\tilde{u}V+m_x\bar{p}\\ \bar{\rho}\tilde{v}V+m_y\bar{p}\\ \bar{\rho}\tilde{w}V+m_z\bar{p}\\ \left(\bar{\rho}\tilde{e}+\bar{p}\right)V-m_t\bar{p}\\ \bar{\rho}\tilde{\nu}V\end{pmatrix},\mathbf{G}=\begin{pmatrix}\bar{\rho}W\\ \bar{\rho}\tilde{u}W+n_x\bar{p}\\ \bar{\rho}\tilde{v}W+n_y\bar{p}\\ \bar{\rho}\tilde{w}W+n_z\bar{p}\\ \left(\bar{\rho}\tilde{e}+\bar{p}\right)W-n_t\bar{p}\\ \bar{\rho}\tilde{\nu}W\end{pmatrix} \tag{2}$$

$$\mathbf{E_v}=\begin{pmatrix}0\\ l_k\bar{\tau}_{xk}\\ l_k\bar{\tau}_{yk}\\ l_k\bar{\tau}_{zk}\\ l_k\left(\tilde{u}_i\bar{\tau}_{ki}-\bar{q}_k\right)\\ \frac{\bar{\rho}}{\sigma}\left(\nu+\tilde{\nu}\right)\left(\mathbf{l}\bullet\nabla\tilde{\nu}\right)\end{pmatrix},\mathbf{F_v}=\begin{pmatrix}0\\ m_k\bar{\tau}u_{xk}\\ m_k\bar{\tau}_{yk}\\ m_k\bar{\tau}u_{zk}\\ m_k\left(\tilde{u}_i\bar{\tau}_{ki}-\bar{q}_k\right)\\ \frac{\bar{\rho}}{\sigma}\left(\nu+\tilde{\nu}\right)\left(\mathbf{m}\bullet\nabla\tilde{\nu}\right)\end{pmatrix},\mathbf{G_v}=\begin{pmatrix}0\\ n_k\bar{\tau}_{xk}\\ n_k\bar{\tau}_{yk}\\ n_k\bar{\tau}_{zk}\\ n_k\left(\tilde{u}_i\bar{\tau}_{ki}-\bar{q}_k\right)\\ \frac{\bar{\rho}}{\sigma}\left(\nu+\tilde{\nu}\right)\left(\mathbf{n}\bullet\nabla\tilde{\nu}\right)\end{pmatrix} \tag{3}$$

$$\mathbf{S}=\frac{1}{J}\begin{pmatrix}0\\ 0\\ 0\\ 0\\ 0\\ S_\nu\end{pmatrix} \tag{4}$$

where $\rho$ is the density, $p$ is the static pressure, and $e$ is the total energy per unit mass. The overbar term denotes a regular filtered variable in the LES region,or a Reynolds-averaged value in the RANS region. And the tilde symbol is used to denote the Favre filtered variable. $\nu$ is kinematic viscosity and $\tilde{\nu}$ is the working variable related to eddy viscosity in S-A and IDDES turbulence one equation model[14]. $U$, $V$ and $W$ are the contravariant velocities in $\xi$, $\eta$, $\zeta$ directions, and defined as

$$
\begin{aligned}
U &= l_t + \mathbf{l} \bullet \mathbf{V} = l_t + l_x\tilde{u} + l_y\tilde{v} + l_z\tilde{w} \\
V &= m_t + \mathbf{m} \bullet \mathbf{V} = m_t + m_x\tilde{u} + m_y\tilde{v} + m_z\tilde{w} \\
W &= n_t + \mathbf{n} \bullet \mathbf{V} = n_t + n_x\tilde{u} + n_y\tilde{v} + n_z\tilde{w}
\end{aligned} \tag{5}
$$

where $J$ is the Jacobian of the coordinate transformation. $l_t$, $m_t$ and $n_t$ are the components of the interface contravariant velocity of the grid in $\xi$, $\eta$ and $\zeta$ directions respectively. $\mathbf{l}$, $\mathbf{m}$ and $\mathbf{n}$ denote the normal vectors located at the centers of $\xi$, $\eta$ and $\zeta$ interfaces of the control volume with their magnitudes equal to the surface areas and pointing to the directions of increasing $\xi$, $\eta$ and $\zeta$.

$$
\mathbf{l} = \frac{\nabla\xi}{J},\ \mathbf{m} = \frac{\nabla\eta}{J},\ \mathbf{n} = \frac{\nabla\zeta}{J} \tag{6}
$$

$$
l_t = \frac{\xi_t}{J},\ m_t = \frac{\eta_t}{J},\ n_t = \frac{\zeta_t}{J} \tag{7}
$$

In the generalized coordinates, $\Delta\xi = \Delta\eta = \Delta\zeta = 1$. Since the DES-family approach is based on S-A model, the formulations of the original S-A model are give below. The source term $S_\nu$ from the S-A model in Eq. (4), is given by

$$
\begin{aligned}
S_\nu = \bar{\rho}C_{b1}\left(1 - f_{t2}\right)\tilde{S}\tilde{\nu} + \tfrac{1}{Re}\Big[-\bar{\rho}\left(C_{w1}f_w - \tfrac{C_{b1}}{\kappa^2}f_{t2}\right)\left(\tfrac{\tilde{\nu}}{d}\right)^2 \\
+ \tfrac{\bar{\rho}}{\sigma}C_{b2}\left(\nabla\tilde{\nu}\right)^2 - \tfrac{1}{\sigma}\left(\nu + \tilde{\nu}\right)\nabla\tilde{\nu} \bullet \nabla\bar{\rho}\Big] + Re\left[\bar{\rho}f_{t1}\left(\Delta q\right)^2\right]
\end{aligned} \tag{8}
$$

where

$$
\chi = \frac{\tilde{\nu}}{\nu}, \quad f_{v1} = \frac{\chi^3}{\chi^3 + c_{v1}^3}, \quad f_{v2} = 1 - \frac{\chi}{1 + \chi f_{v1}}, \quad f_{t1} = C_{t1}g_t exp\left[-C_{t2}\frac{\omega_t^2}{\Delta U^2}\left(d^2 + g_t^2 d_t^2\right)\right] \tag{9}
$$

$$
f_{t2} = C_{t3}exp\left(-C_{t4}\chi^2\right), \quad f_w = g(\frac{1 + c_{w3}^6}{g^6 + c_{w3}^6})^{1/6}, \quad g = r + c_{w2}(r^6 - r) \tag{10}
$$

$$
g_t = min\left(0.1, \frac{\Delta q}{\omega_t \Delta x_t}\right), \quad \tilde{S} = S + \frac{\tilde{\nu}}{k^2 d^2 R_e}f_{v2}, \quad r = \frac{\tilde{\nu}}{\tilde{S}k^2 d^2 R_e} \tag{11}
$$

where, $\omega_t$ is the wall vorticity at the wall boundary layer trip location, $d$ is the distance to the closest wall, $d_t$ is the distance of the field point to the trip location, $\Delta q$ is the difference of the velocities between the field point and the trip location, $\Delta x_t$ is the grid spacing along the wall at the trip location. The values of the coefficients are: $c_{b1} = 0.1355, c_{b2} = 0.622, \sigma = \frac{2}{3}, c_{w1} = \frac{c_{b1}}{k^2} + (1 + c_{b2})/\sigma, c_{w2} = 0.3, c_{w3} = 2, k = 0.41, c_{v1} = 7.1, c_{t1} = 1.0, c_{t2} = 2.0, c_{t3} = 1.1, c_{t4} = 2.0$.

The shear stress $\bar{\tau}_{ik}$ and total heat flux $\bar{q}_k$ in Cartesian coordinates is given by

$$
\bar{\tau}_{ik} = \left(\mu + \mu_{IDDES}\right)\left[\left(\frac{\partial\tilde{u}_i}{\partial x_k} + \frac{\partial\tilde{u}_k}{\partial x_i}\right) - \frac{2}{3}\delta_{ik}\frac{\partial\tilde{u}_j}{\partial x_j}\right] \tag{12}
$$

$$
\bar{q}_k = -\left(\frac{\mu}{Pr} + \frac{\mu_{IDDES}}{Pr_t}\right)\frac{\partial\tilde{T}}{\partial x_k} \tag{13}
$$

where $\mu$ is from Sutherland's law. For IDDES approach in general, the eddy viscosity is represented by $\mu_{IDDES}(= \bar{\rho}\tilde{\nu}f_{v1})$.

## 2.2 Improved Delayed Detached Eddy Simulation(IDDES)

The Improved DDES(IDDES) is introduced by extending the DDES with the WMLES capacity. The IDDES has two branches, DDES and WMLES, including a set of empirical functions of subgrid length-scales designed to achieve good performance from these branches themselves and their coupling. By switching the activation of RANS and LES in different flow regions, IDDES significantly expands the scope of application of DDES with well-balanced and powerful numerical approach to complex turbulent flows at high Reynolds numbers.

The three aspects of IDDES are presented below: the DDES branch , the WMLES branch and hybridization of DDES and WMLES.

### DDES branch of IDDES

This branch is responsible for the DDES-like functionality of IDDES and should become active only when the inflow conditions do not have any turbulent content (if a simulation has spatial periodicity, the initial conditions rather than the inflow conditions set the characteristics of the simulation), in particular when a grid of "boundary-layer type" precludes the resolution of the dominant eddies. The DDES formulation can be reformulated as

$$l_{DDES} = l_{RANS} - f_d max\{0, l_{RANS} - l_{LES}) \tag{14}$$

where the delaying function, $f_d$, is defined the same as

$$f_d = 1 - tanh[(8r_d)^3] \tag{15}$$

and the quantity $r_d$ borrowed from the S-A RANS turbulence model:

$$r_d = \frac{\nu_t + \nu}{k^2 d_w^2 max[(U_{i,j}U_{i,j})^{0.5}, 10^{-10}]} \tag{16}$$

is a marker of the wall region, which is equal to 1 in a log layer and 0 in a free shear flow.

In Eq. (16), $U_{i,j}$ represents the velocity gradient, and $k$ denotes the Karmann constant. Based on the general DES concept, in order to create a seamless hybrid model, the length-scale IDDES defined by Eq.14 is substituted into the background RANS model to replace the RANS length-scale, $l_{RANS}$, which is explicitly or implicitly involved in any such model. For instance, for the S-A model the length-scale is equal to the distance to the wall $l_{RANS} = d_w$. In the original DES97, the length-scale depends only on the local grid. In DDES and IDDES, it also depends on the solution of Eq. (14) and (16).

As far as the LES length-scale, $l_{LES}$, in Eq. (14) is concerned, it is defined via the subgrid length-scale as

$$l_{LES} = C_{DES}\Phi\Delta \tag{17}$$

where $C_{DES}$ is the fundamental empirical constant of DES, 0.65. $\Phi$ is a low-Reynolds number correction introduced in order to compensate the activation of the low-Reynolds number terms of some background RANS model in LES mode. Both $C_{DES}$ and $\Phi$ depend on the background RANS model, and $\Psi$ is equal to 1 if the RANS model does not include any low-Reynolds number terms.

### WMLES branch of IDDES

This branch is intended to be active only when the inflow conditions used in the simulation are unsteady and impose some turbulent content with the grid fine enough to resolve boundary-layer dominant eddies. It presents a new seamless hybrid RANS-LES model, which couples RANS and LES approaches via the introduction of the following blended RANS-LES length-scale:

$$l_{WMLES} = f_B(1 + f_e)l_{RANS} + (1 - f_B)l_{LES} \tag{18}$$

The empirical blending-function $f_B$ depends upon $d_w/h_{max}$ and is defined as

$$f_B = min\{2exp(-9\alpha^2), 1.0\}, \alpha = 0.25 - d_w/h_{max} \tag{19}$$

It varies from 0 to 1 and provides rapid switching of the model from RANS mode ($f_B = 1.0$) to LES mode ($f_B = 0$) within the range of wall distance $0.5h_{max} < d_w < h_{max}$

The second empirical function involved in Eq. (18), elevating-function, $f_e$, is aimed at preventing the excessive reduction of the RANS Reynolds stresses observed in the interaction of the RANS and LES regions in the vicinity of their interface. It is intended to eliminating the log-layer mismatch(LLM) problem.

$$f_e = max\{(f_{e1} - 1), 0\}\Phi f_{e2} \tag{20}$$

where the function $f_{e1}$ is defined as

$$f_{e1}(d_w/h_{max}) = \begin{cases} 2exp(-11.09\alpha^2) & \text{if } \alpha \geq 0 \\ 2exp(-9.0\alpha^2) & \text{if } \alpha < 0 \end{cases} \tag{21}$$

It provides a grid-dependent "elevating device for the RANS component of the WMLES length-scale.

The function $f_{e2}$ is:

$$f_{e2} = 1.0 - max\{f_t, f_l\} \tag{22}$$

**Blending DDES and WMLES branches**

The DDES length-scale defined by Eq. (14) and that of the WMLES-branch defined by Eq. (18) do not blend directly in a way to ensure an automatic choice of the WMLES or DDES mode by the combined model, depending on the type of the simulation (with or without turbulent content) and the grid used.

However a modified version of equivalent length scale combination, namely,

$$\tilde{l}_{DDES} = \tilde{f}_d l_{RANS} + (1 - \tilde{f}_d)l_{LES} \tag{23}$$

where the blending function $\tilde{f}_d$ is defined by

$$\tilde{f}_d = max\{(1 - f_{dt}), f_B\} \tag{24}$$

with $f_{dt} = 1 - tanh[(8r_{dt})^3]$

With the use of Eq. (23), the required IDDES length-scale combining the DDES and WMLES length scales defined by Eq. (23) and (18) is straightforward and can be implemented as

$$l_{hyb} = \tilde{f}_d(1 + f_e)l_{RANS} + (1 - \tilde{f}_d)l_{LES} \tag{25}$$

With inflow turbulent content, $f_{dt}$ is close to 1.0, $\tilde{f}_d$ is equal to $f_B$, so Eq. (25) is reducted to $l_{hyb} = l_{WMLES}$ in Eq. (18). Otherwise, $f_e$ is zero, Eq. (25) is interpreted as $l_{hyb} = l_{DDES}$ in Eq. (23)

### 2.3 Time Marching Scheme

Following the dual time stepping method suggested by Jameson[15], an implicit pseudo time marching scheme using line Gauss-Seidel line relaxation is employed to solve the governing equations, as the following:

$$\frac{\partial \mathbf{Q}}{\partial t} = \frac{\mathbf{3Q^{n+1} - 4Q^{n} + Q^{n-1}}}{2\Delta t} \tag{26}$$

where $n-1$, $n$ and $n+1$ are three sequential time levels, which have a time interval of $\Delta t$. The first-order Euler scheme is used to discretize the pseudo temporal term. The semi-discretized equations of the governing equations are given as the following:

$$\begin{aligned} &\left[\left(\tfrac{1}{\Delta\widehat{\tau}} + \tfrac{1.5}{\Delta t}\right) I - \left(\tfrac{\partial R}{\partial \mathbf{Q}}\right)^{n+1,m}\right] \delta\mathbf{Q^{n+1,m+1}} \\ &\quad = R^{n+1,m} - \tfrac{\mathbf{3Q^{n+1,m} - 4Q^{n} + Q^{n-1}}}{2\Delta t} \end{aligned} \tag{27}$$

where the $\Delta\widehat{\tau}$ is the pseudo time step, and R stands for the net flux determined by the spatial high order numerical scheme, $m$ is the iteration index for the pseudo time.

### 2.4 The Low Diffusion E-CUSP Scheme

The Low Diffusion E-CUSP(LDE) Scheme[16] is employed to calculate the inviscid fluxes. The key concept of LDE scheme is to split the inviscid flux into convective $E^c$ and a pressure $E^p$ based on characteristics analysis. In generalized coordinate system, the flux $\mathbf{E}$ can be split as the following:

$$\mathbf{E}' = E^c + E^p = \begin{pmatrix} \rho U \\ \rho u U \\ \rho v U \\ \rho w U \\ \rho e U \\ \rho \tilde{\nu} U \end{pmatrix} + \begin{pmatrix} 0 \\ \xi_x p \\ \xi_y p \\ \xi_z p \\ p\overline{U} \\ 0 \end{pmatrix} \tag{28}$$

where, $U$ is the contravariant velocity as defined in Eq. (5). $\overline{U}$ is defined as:

$$\overline{U} = U - \xi_t = \xi_x u + \xi_y v + \xi_z w \tag{29}$$

The convective flux, $E^c$ is evaluated by

$$E^c = \rho U \begin{pmatrix} 1 \\ u \\ v \\ w \\ e \\ \tilde{\nu} \end{pmatrix} = \rho U f^c,\ f^c = \begin{pmatrix} 1 \\ u \\ v \\ w \\ e \\ \tilde{\nu} \end{pmatrix} \tag{30}$$

Let

$$C = c\left(\xi_x^2 + \xi_y^2 + \xi_z^2\right)^{\frac{1}{2}} \tag{31}$$

where $c = \sqrt{\gamma RT}$ is the speed of sound. Then the convective flux at interface $i + \frac{1}{2}$ is evaluated as:

$$E^c_{i+\frac{1}{2}} = C_{\frac{1}{2}}\left[\rho_L C^+ f^c_L + \rho_R C^- f^c_R\right] \tag{32}$$

where, the subscripts $L$ and $R$ represent the left and right hand sides of the interface. The Mach number splitting of Edwards[17] is borrowed to determine $C^+$ and $C^-$ as the following:

$$C_{\frac{1}{2}} = \frac{1}{2}\left(C_L + C_R\right) \tag{33}$$

$$C^+ = \alpha^+_L\left(1 + \beta_L\right) M_L - \beta_L M^+_L - M^+_{\frac{1}{2}} \tag{34}$$

$$C^- = \alpha^-_R\left(1 + \beta_R\right) M_R - \beta_R M^-_R + M^-_{\frac{1}{2}} \tag{35}$$

$$M_L = \frac{U_L}{C_{\frac{1}{2}}},\ M_R = \frac{U_R}{C_{\frac{1}{2}}} \tag{36}$$

$$\alpha_{L,R} = \frac{1}{2}\left[1 \pm sign\left(M_{L,R}\right)\right] \tag{37}$$

$$\beta_{L,R} = -max\left[0, 1 - int\left(|M_{L,R}|\right)\right] \tag{38}$$

$$M^+_{\frac{1}{2}} = M_{\frac{1}{2}}\frac{C_R + C_L\Phi}{C_R + C_L} \tag{39}$$

$$M^-_{\frac{1}{2}} = M_{\frac{1}{2}}\frac{C_L + C_R\Phi^{-1}}{C_R + C_L} \tag{40}$$

$$\Phi = \frac{\left(\rho C^2\right)_R}{\left(\rho C^2\right)_L} \tag{41}$$

$$M_{\frac{1}{2}} = \beta_L\delta^+ M^-_L - \beta_R\delta^- M^+_R \tag{42}$$

$$M^\pm_{L,R} = \pm\frac{1}{4}\left(M_{L,R} \pm 1\right)^2 \tag{43}$$

$$\delta^\pm = \frac{1}{2}\left\{1 \pm sign\left[\frac{1}{2}\left(M_L + M_R\right)\right]\right\} \tag{44}$$

The pressure flux, $E^p$ is evaluated as the following

$$E^p_{i+\frac{1}{2}} = \begin{pmatrix} 0 \\ \mathcal{P}^+ p\,\xi_x \\ \mathcal{P}^+ p\,\xi_y \\ \mathcal{P}^+ p\,\xi_z \\ \frac{1}{2}p\left[\overline{U}+\overline{C}_{\frac{1}{2}}\right] \\ 0 \end{pmatrix}_L + \begin{pmatrix} 0 \\ \mathcal{P}^- p\,\xi_x \\ \mathcal{P}^- p\,\xi_y \\ \mathcal{P}^- p\,\xi_z \\ \frac{1}{2}p\left[\overline{U}-\overline{C}_{\frac{1}{2}}\right] \\ 0 \end{pmatrix}_R \tag{45}$$

The contravariant speed of sound $\overline{C}$ in the pressure vector is consistent with $\overline{U}$. It is computed based on $C$ as the following,

$$\overline{C} = C - \xi_t \tag{46}$$

The use of $\overline{U}$ and $\overline{C}$ instead of $U$ and $C$ in the pressure vector is to take into account of the grid speed so that the flux will transit from subsonic to supersonic smoothly. When the grid is stationary, $\xi_t = 0$, $\overline{C} = C$, $\overline{U} = U$. The pressure splitting coefficient is:

$$\mathcal{P}^{\pm}_{L,R} = \frac{1}{4}\left(M_{L,R} \pm 1\right)^2 \left(2 \mp M_L\right) \tag{47}$$

The LDE scheme can capture crisp shock profile and exact contact surface discontinuities as accurately as the Roe scheme[16].

### 2.5 The 5th Order WENO Scheme

For reconstruction of the interface flux, $E_{i+\frac{1}{2}} = E(Q_L, Q_R)$, the conservative variables $Q_L$ and $Q_R$ are evaluated by using the 5th order WENO scheme[18, 19]. For example,

$$(Q_L)_{i+\frac{1}{2}} = \omega_0 q_0 + \omega_1 q_1 + \omega_2 q_2 \tag{48}$$

where

$$q_0 = \frac{1}{3}Q_{i-2} - \frac{7}{6}Q_{i-1} + \frac{11}{6}Q_i \tag{49}$$

$$q_1 = -\frac{1}{6}Q_{i-1} + \frac{5}{6}Q_i + \frac{1}{3}Q_{i+1} \tag{50}$$

$$q_2 = \frac{1}{3}Q_i + \frac{5}{6}Q_{i+1} - \frac{1}{6}Q_{i+2} \tag{51}$$

$$\omega_k = \frac{\alpha_k}{\alpha_0 + \ldots + \alpha_{r-1}} \tag{52}$$

$$\alpha_k = \frac{C_k}{\epsilon + IS_k},\ k = 0, \ldots, r-1 \tag{53}$$

$$C_0 = 0.1,\ C_1 = 0.6,\ C_2 = 0.3 \tag{54}$$

$$IS_0 = \frac{13}{12}\left(Q_{i-2} - 2Q_{i-1} + Q_i\right)^2 + \frac{1}{4}\left(Q_{i-2} - 4Q_{i-1} + 3Q_i\right)^2 \tag{55}$$

$$IS_1 = \frac{13}{12}\left(Q_{i-1} - 2Q_i + Q_{i+1}\right)^2 + \frac{1}{4}\left(Q_{i-1} - Q_{i+1}\right)^2 \tag{56}$$

$$IS_2 = \frac{13}{12}\left(Q_i - 2Q_{i+1} + Q_{i+2}\right)^2 + \frac{1}{4}\left(3Q_i - 4Q_{i+1} + Q_{i+2}\right)^2 \tag{57}$$

$\epsilon$ is originally introduced to avoid the denominator becoming zero and is supposed to be a very small number. In [19], it is observed that $IS_k$ will oscillate if $\epsilon$ is too small and also shift the weights away from the optimal values in the smooth region. The higher the $\epsilon$ values, the closer the weights approach the optimal values, $C_k$, which will give the symmetric evaluation of the interface flux with minimum numerical dissipation. When there are shocks in the flow field, $\epsilon$ can not be too large to maintain the sensitivity to shocks. In [19], $\epsilon = 10^{-2}$ is recommended for the transonic flow with shock waves. In the current work since there is no shock in the flow, the $\epsilon = 0.3$ is used.

The viscous terms are discretized by a fully conservative fourth-order accurate finite central differencing scheme suggested by Shen et al. [20, 21].

### 2.6 Boundary Conditions

Steady state freestream conditions including total pressure, total temperature, and two flow angles are specified for the upstream portion of the far field boundary. For far field downstream boundary, the static pressure is specified as freestream value to match the intended freestream Mach number. The streamwise gradients of other variables are forced to vanish. The periodic boundary condition is used in spanwise direction. The wall treatment suggested in [19] to achieve flux conservation by shifting half interval of the mesh on the wall is employed. If the wall surface normal direction is in $\eta$-direction, the no slip condition is enforced on the surface by computing the wall inviscid flux $F_{1/2}$ in the following manner:

$$\mathbf{F_w} = \begin{pmatrix} \rho V \\ \rho u V + p\eta_x \\ \rho v V + p\eta_y \\ \rho w V + p\eta_z \\ (\rho e + p)V \end{pmatrix}_w = \begin{pmatrix} 0 \\ p\eta_x \\ p\eta_y \\ p\eta_z \\ 0 \end{pmatrix}_w \tag{58}$$

## 3 CFJ Parameters

This section gives the important parameters to evaluate a CFJ airfoil performance.

### 3.1 Lift and Drag Calculation

The momentum and pressure at the injection and suction slots produce a reactionary force, which is automatically measured by the force balance in wind tunnel testing. However, for CFD simulation, the full reactionary force needs to be included. Using control volume analysis, the reactionary force can be calculated using the flow parameters at the injection and suction slot opening surfaces. Zha et al. [3] give the following formulations to calculate the lift and drag due to the jet reactionary force for a CFD simulation. By considering the effects of injection and suction jets on the CFJ airfoil, the expressions for these reactionary forces are given as :

$$F_{x_{cfj}} = (\dot{m}_j V_{j1} + p_{j1} A_{j1}) * \cos(\theta_1 - \alpha) - (\dot{m}_j V_{j2} + p_{j2} A_{j2}) * \cos(\theta_2 + \alpha) \tag{59}$$

$$F_{y_{cfj}} = (\dot{m}_{j1} V_{j1} + p_{j1} A_{j1}) * \sin(\theta_1 - \alpha) + (\dot{m}_{j2} V_{j2} + p_{j2} A_{j2}) * \sin(\theta_2 + \alpha) \tag{60}$$

where the subscripts 1 and 2 stand for the injection and suction respectively, and $\theta_1$ and $\theta_2$ are the angles between the injection and suction slot surfaces and a line normal to the airfoil chord. $\alpha$ is the angle of attack.

The total lift and drag on the airfoil can then be expressed as:

$$D = R'_x - F_{x_{cfj}} \tag{61}$$

$$L = R'_y - F_{y_{cfj}} \tag{62}$$

where $R'_x$ and $R'_y$ are the surface integral of pressure and shear stress in $x$ (drag) and $y$ (lift) direction excluding the internal ducts of injection and suction. For the CFD simulation, the total lift and drag are calculated using Eqs. (61) and (62).



## 3.2 Jet Momentum Coefficient

The jet momentum coefficient $C_\mu$ is a parameter used to quantify the injection intensity. It is defined as :

$$C_\mu = \frac{\dot{m} V_j}{\frac{1}{2}\rho_\infty {V_\infty}^2 S} \tag{63}$$

where $\dot{m}$ is the injection mass flow, $V_j$ the injection velocity, $\rho_\infty$ and $V_\infty$ denote the free stream density and velocity, and S is the platform area.

### 3.2.1 $C_\mu$ Iteration:

To achieve zero net mass flux with the CFJ flow control, the mass flow exiting the injection slot must be equal to the mass flow entering the suction slot, i.e. $\dot{m}_{inj} = \dot{m}_{suc}$. The prescribed jet momentum coefficient $C_\mu$ is achieved by adjusting the injection cavity total pressure. Total temperature is assumed constant during this process. The injection and suction mass flow rates are matched by adjusting the suction cavity static pressure. The iterative process is conducted throughout the simulation until the specified momentum coefficient is reached and the injection and suction mass flow match within the acceptable tolerance, which is 0.2% for the present study.

## 3.3 Power Coefficient

The CFJ can be implemented by mounting a pumping system inside the wing that withdraws air from the suction slot and blows it into the injection slot. The power consumption can be determined by the jet mass flow and total enthalpy change as the following :

$$P = \dot{m}(H_{t1} - H_{t2}) \tag{64}$$

where $H_{t1}$ and $H_{t2}$ are the total enthalpy in the injection cavity and suction cavity respectively, $P$ is the Power required by the pump and $\dot{m}$ the jet mass flow rate. Introducing the pumping efficiency $\eta$ and total pressure ratio of the pump $\Gamma = \frac{P_{t1}}{P_{t2}}$, the power consumption can be expressed as :

$$P = \frac{\dot{m} C_p T_{t2}}{\eta}(\Gamma^{\frac{\gamma-1}{\gamma}} - 1) \tag{65}$$

The power consumption can be expressed as a power coefficient below:

$$P_c = \frac{P}{\frac{1}{2}\rho_\infty V_\infty^3 S} \tag{66}$$

In this research, the pumping efficiency of 100% is used for all the simulations unless indicated otherwise.

### 3.4 Corrected Aerodynamic Efficiency

The conventional airfoil aerodynamic efficiency is defined as $\frac{L}{D}$. However since CFJ active flow control consumes energy, the CFJ corrected aerodynamic efficiency is modified to take into account the energy consumption of the pump. The formulation of the corrected aerodynamic efficiency for CFJ airfoils is :

$$(\frac{L}{D})_c = \frac{L}{D + \frac{P}{V_\infty}} = \frac{C_L}{C_D + P_C} \tag{67}$$

where $V_\infty$ is the free stream velocity, $P$ is the CFJ pumping power, and $L$ and $D$ are the lift and drag generated by the CFJ airfoil. This formulation converts the power consumed by the CFJ into the drag of the airfoil. If the pumping power is set to 0, this formulation returns to the aerodynamic efficiency of a conventional airfoil.

## 4 Aircraft Productivity

The transportation ability of an airplane is measured by how much total weight the aircraft can move for the maximum distance. We use a term "productivity" defined as the product of the total weight by the maximum range to represent the transportation ability of an airplane.

For a jet engine airplane, the total weight of the aircraft decreases during flight. A non-dimensional productivity parameter is hence defined using the aircraft averaged weight as below:

$$C_{RW} = \frac{R\overline{W}}{\frac{1}{2c_t}\bar{\rho}V_\infty^3 S} = \frac{C_L^2}{C_D}\ln\frac{W_0}{W_f} \tag{68}$$

where $R$ is the aircraft range, $\overline{W}$ is the averaged weight of the aircraft during cruise, $c_t$ is the engine cruise thrust specific fuel consumption[fuel weight(N)/(thrust(N) s)], $\bar{\rho}$ is the averaged air density during cruise due to altitude variation, $S$ is the wing platform area, $W_0$ is the aircraft initial gross weight at takeoff, $W_f$ is the final weight at landing. This formulation is obtained from the Breguet Range Equation. The productivity parameter represents the productivity of the aircraft with the fuel consumed per unit time.

For a propeller engine airplane, the productivity parameter is defined as:

$$C_{RW} = \frac{R\overline{W}}{\frac{1}{2c}\bar{\rho}V_\infty^2 S} = \eta\frac{C_L^2}{C_D}\ln\frac{W_0}{W_f} \tag{69}$$

where $c$ is the fuel specific consumption of the propeller engine[fuel weight(N)/(BHP(W) s)], $\eta$ is the propeller efficiency.

For a full electric battery powered propeller airplane, the aircraft weight will not change during flight. The productivity parameter is defined as:

$$C_{RW} = \frac{RW}{\frac{1}{2c}\rho V_\infty^2 S E_c/g} = \eta \frac{C_L^2}{C_D}\frac{W_b}{W_0} \tag{70}$$

where $E_c$ is the battery specific energy density (Wh/kg), $W_b$ is the total battery weight.

To compare aircraft that have the same ratio of initial weight to final weight with the same engine fuel consumption or battery energy density, the only factor affecting their productivity parameter is $C_L^2/C_D$. We hence name $C_L^2/C_D$ as productivity efficiency.

We consider the productivity efficiency $C_L^2/C_D = C_L(C_L/C_D)$ as a more comprehensive parameter than the conventional aerodynamic efficiency $C_L/C_D$ to measure the merit of an airplane aerodynamic design for cruise performance. The former includes not only the information of $C_L/C_D$, but also the information of the aircraft weight $C_L$. For example, for two airplane designs having the same $C_L/C_D$ with one $C_L$ twice larger than the other, if the wing sizes are the same, one airplane will be able to carry twice more weight than the other with productivity and wing loading increased by 100%. Such a large difference is not reflected by $C_L/C_D$, but very well reflected by $C_L^2/C_D$.

The definition of $C_L/C_D$ in general is a suitable measure of merit for conventional aircraft design. This is because at a certain Mach number regime, the maximum $C_L/C_D$ is usually achieved at low angle of attack within the drag bucket and is more or less the same for different airfoil designs. In other words, for the same optimum $C_L/C_D$, the $C_L$ is about the same. A typical $C_L$ for subsonic airfoil is about 0.4 and for transonic airfoil is about 0.7.

For CFJ airfoil, the minimum CFJ pumping power occurs at a fairly high AoA as shown in Fig. **??** [9, 11]. With the augmentation of CFJ, the subsonic cruise lift coefficient of a CFJ airfoil is typically 2 to 3 times higher than the conventional airfoil with about the same $(C_L/C_D)_c$ [22]. Such a high lift coefficient is unattainable for conventional airfoil since they would be either stalled or near stalled with very high drag. Hence for CFJ aircraft design, the productivity efficiency $C_L^2/C_D = C_L(C_L/C_D)$ is more informative to be used to reflect the aerodynamic performance. The corrected productivity efficiency for CFJ airfoils is $(C_L^2/C_D)_c = C_L^2/(C_D + P_c)$.

# 5 Results and Discussion

## 5.1 Computational Mesh and Flow Conditions

The 3D multiblock structured meshes are constructed using the O-mesh topology in order to achieve high mesh quality near airfoil wall surfaces. The total number of 2001 grid points are placed around the airfoil, 601 points on the lower surface, 1401 points on the upper surface, 181 points normal to the airfoil, and 51 points in the spanwise direction. For the CFJ flow domain, an additional 41 points across the jet is placed in the CFJ injection and suction slot. The total mesh size is 20,880,000 cells and is partitioned into 348 blocks for parallel computation. The far-field boundary is located 15 chords away from the airfoil. The CFJ wing span is 0.1 chord with the periodic boundary conditions applied in the spanwise direction. To resolve the turbulent boundary layer, the first grid point is placed at $y^+ \approx 1$. The mesh block information is available in Table 2 and the mesh topology is shown in Fig. 3.

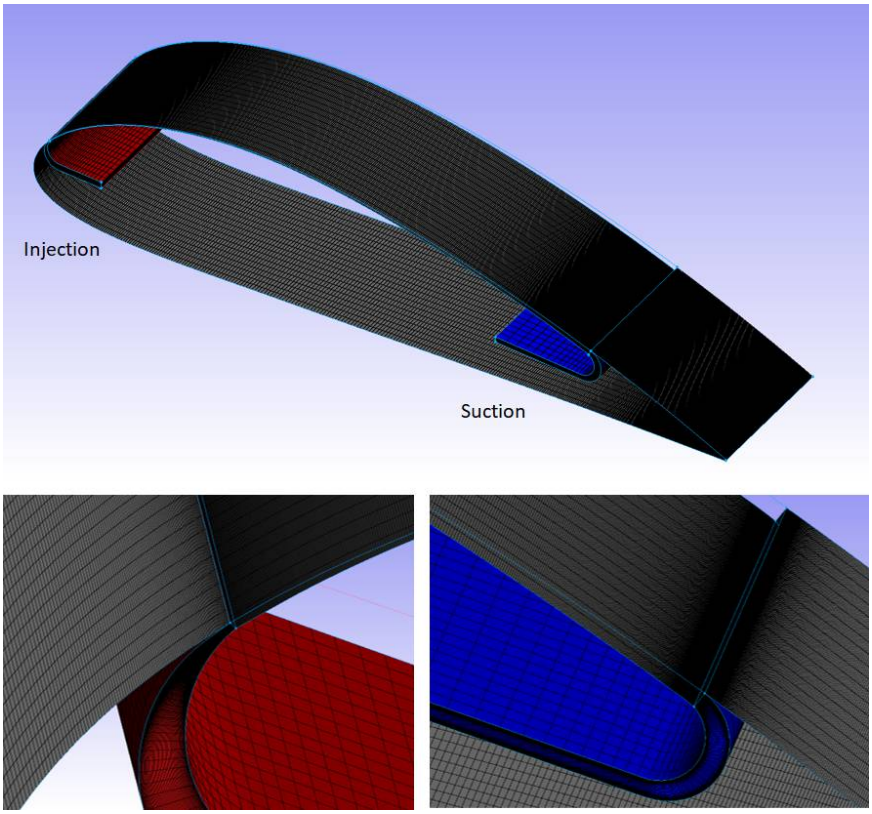


Figure 3: Computational mesh for IDDES calculation

Table 1: Computational parameters for the flat plate validation

| cases | Mach | Reynolds | Mesh $N_\xi \times N_\eta \times N_\zeta$ | $\Delta x$ | $\Delta y_1$ | $\Delta z$ | $\Delta x^+$ | $\Delta y_1^+$ | $\Delta z^+$ |
|---|---|---|---|---|---|---|---|---|---|
| baseline | 0.028 | 480,000 | $2000 \times 180 \times 50$ | 0.001 | $5.0e^{-6}$ | 0.002 | 33.3 | 0.17 | 66.6 |
| CFJ | 0.028 | 480,000 | $2000 \times 180 \times 50^*$ | 0.001 | $5.0e^{-6}$ | 0.002 | 33.3 | 0.17 | 66.6 |

*The grid points around the airfoil exclude the CFJ injection connection, and suction blocks.

Table 2: Mesh details for CFJ 6421

| Block | $\xi$-Direction | $\eta$-Direction | $\zeta$-Direction | Cell number | location |
|---|---|---|---|---|---|
| 1-300 | 20 | 60 | 50 | 60000 | around the airfoil |
| 301-304 | 20 | 60 | 50 | 60000 | Injection block |
| 305-344 | 20 | 60 | 50 | 60000 | Connection |
| 345-348 | 20 | 60 | 50 | 60000 | Suction block |
| Total mesh size | | | | 20,880,000 | |

The CFJ airfoil configurations are created from the baseline NACA 6421 airfoil by translating the suction surface downward, which is defined as the suction surface translation (SST). The CFJ injection and suction slot sizes are obtained by 2D trade study to achieve high lift coefficient for take-off and landing and high cruise efficiency. Fig. 4 shows the illustration of CFJ airfoil parameters, i.e., SSTs, injection slot sizes and suction slot sizes [1].

Table 3 gives the detailed parameters of the CFJ airfoil designed for takeoff/landing including the injection and

Table 3: CFJ-NACA6421 airfoil geometry parameters for takeoff/landing and cruise condition

| Case | CFJ-NACA6421 airfoil | SST (%C) | INJ slot size (%C) | SUC slot size (%C) |
|---|---|---|---|---|
| Takeoff/Landing | SST016-SUC053-INJ009 | 0.16 | 0.09 | 0.53 |

suction slot size normalized by chord length(C), and the injection jet momentum coefficient used. The 3-digit number in the naming convention stands for the SST distance, injection slot size, and suction slot size normalized by the airfoil chord.

For the IDDES simulation, the normalized physical time step of 0.02 and the CFL number of 5 is applied for the pseudo time are used. For the low-speed takeoff/landing simulation, the Mach number is 0.028 and Reynolds number is $4.8 \times 10^5$ based on the freestream velocity of 10 m/s. The jet momentum coefficients $C_\mu$= 0.25, 0.35, and 0.50 are selected for the study to obtain the flow structures that can sustain the super-lift coefficient. The simulated angle of attack is set at 62°. The simulation parameters can be found in table 4.



## 5.2 CFJ wing at AoA of 62°

Table 4: Takeoff/Landing simulation parameters

| CFJ NACA6421 airfoil | $V_{inf}$ | Mach number | Reynolds number | AoA | $C_\mu$ |
|---|---|---|---|---|---|
| SST016-SUC053-INJ009 | 10m/s | 0.028 | 480,000 | 62 | 0.25 |
| SST016-SUC053-INJ009 | 10m/s | 0.028 | 480,000 | 62 | 0.35 |
| SST016-SUC053-INJ009 | 10m/s | 0.028 | 480,000 | 62 | 0.50 |

Table 5: Time-avaraged simulation results

| CFJ6421 airfoil | AoA | $C_\mu$ | $C_L$ | $C_D$ |
|---|---|---|---|---|
| SST016-SUC053-INJ009 | 62 | 0.25 | 6.72 | 0.08 |
| SST016-SUC053-INJ009 | 62 | 0.35 | 8.58 | 0.04 |
| SST016-SUC053-INJ009 | 62 | 0.50 | 9.1 | 0.21 |

The lift and drag coefficient history for AoA=62° and $C_\mu$= 0.5 is shown in Fig. 5. To obtain the desired $C_\mu$, an iterative method is used to calculate the total pressure $P_{tinj}$ at the injection cavity. The static pressure $P_{ssuc}$ at the suction cavity is computed in the same way to maintain the mass conservation of the CFJ injection and suction. The lift and drag curve are gradually converged to a stable oscillation around the mean value of $C_L$ and $C_D$ after the characteristic time $\bar{t} \approx 200$. The time-averaged lift coefficient is 9.1 and the time-averaged drag coefficient is 0.21. Similar lift and drag coefficient history with physical time iteration is found for the other $C_\mu$, the summarized time-averaged result is in table 5.

Fig. 6 is the streamlines for the CFJ airfoil at AoA = 62 ° and $C_\mu = 0.50$. The streamlines show that the flow is well attached to the airfoil, which indicates that the flow goes around the airfoil from the trailing edge towards the leading edge on the lower surface and turns back toward the trailing edge on the upper surface. Then the flow direction changes nearly 180° at the leading edge with suction peak velocity. The main flow then mixes with the high momentum CFJ jet and leaves the wing surface near the trailing edge. The predicted 3D flow field is different from the 2D airfoil flow in that the spanwise vortical flow structures exist. Besides, the IDDES simulation indicates that flow is mildly separated near the trailing edge on the upper surface. Given the three-dimensional

turbulent flow features, the exact location of the stagnation point can not be clearly identified as the 2D RANS simulation.

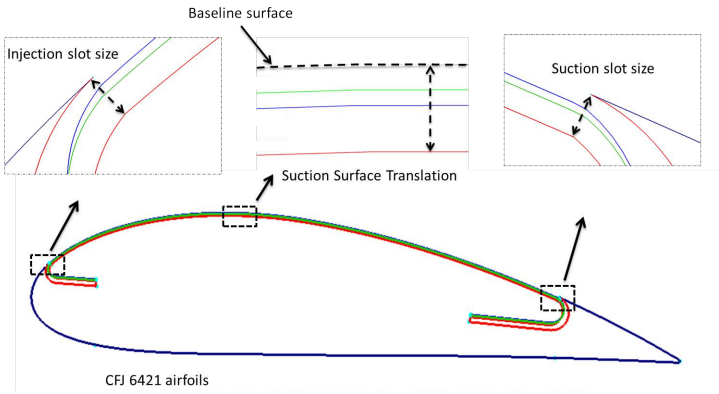


Figure 4: CFJ6421 airfoil geometry parameters.

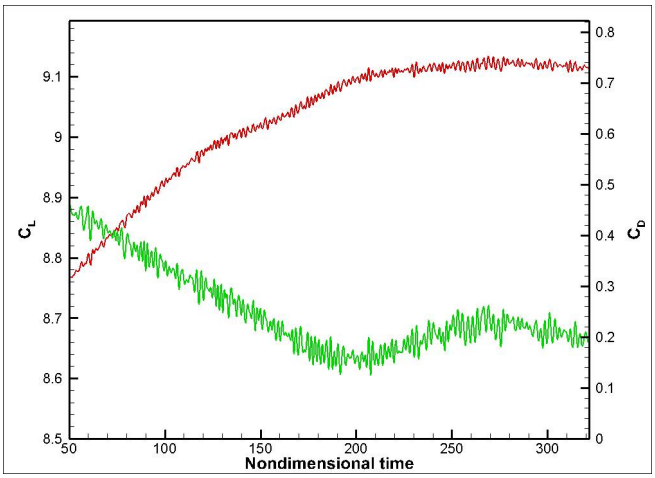


Figure 5: Lift and drag coefficient history at AoA = 62 ° and $C\mu = 0.5$.

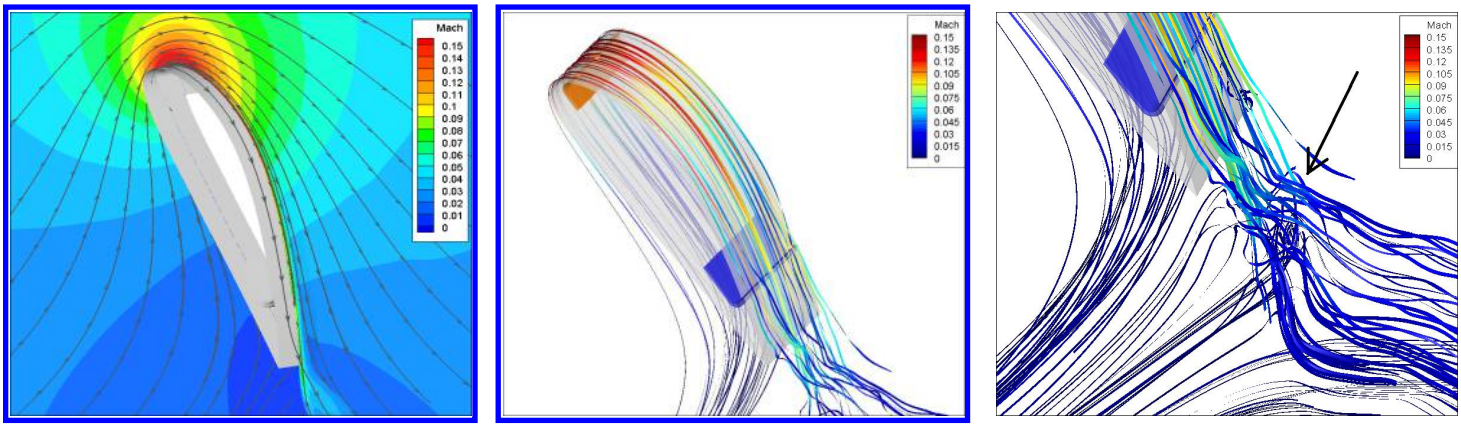


Time-averaged streamlines | Instantaneous streamlines | near trailing edge

Figure 6: The time-averaged and instantaneous streamlines and Mach number contours at AoA = 62 ° and $C_\mu$ = 0.5.

The time-averaged and instantaneous Mach contours and streamlines of the CFJ wing at AoA = 62° and $C_\mu$ = 0.5 are shown in Fig. 6. The time-averaged streamlines indicate that the flow is well attached to the surface throughout the airfoil surface. Therefore, the CFJ flow control can greatly enhance the maximum achievable lift by making the flow attached to the wing. The high-speed velocity region is observed near the leading edge with the peak Mach number up to 0.15. The flow acceleration near the leading edge creates a very pressure region, which contributes to the high lift enhancement.

Fig. 7 shows the time-averaged Mach number contours of the CFJ wing at AoA = 62° and different $C_\mu$ of 0.25, 0.35, and 0.5. All the Mach number contours show that the high-speed flow field near the leading edge. This Mach is much higher than the free stream Mach number of 0.028. The local pressure field is significantly reduced due to the flow acceleration. The CFJ jet emanated from the injection slot creates the high-speed jet throughout the upper surface. For $C_\mu$ greater than 0.35, the high speed jet due to CFJ is maintained up to the trailing edge, whereas at $C_\mu$=0.25, the high speed jet is terminated by a small flow separation at trailing edge.

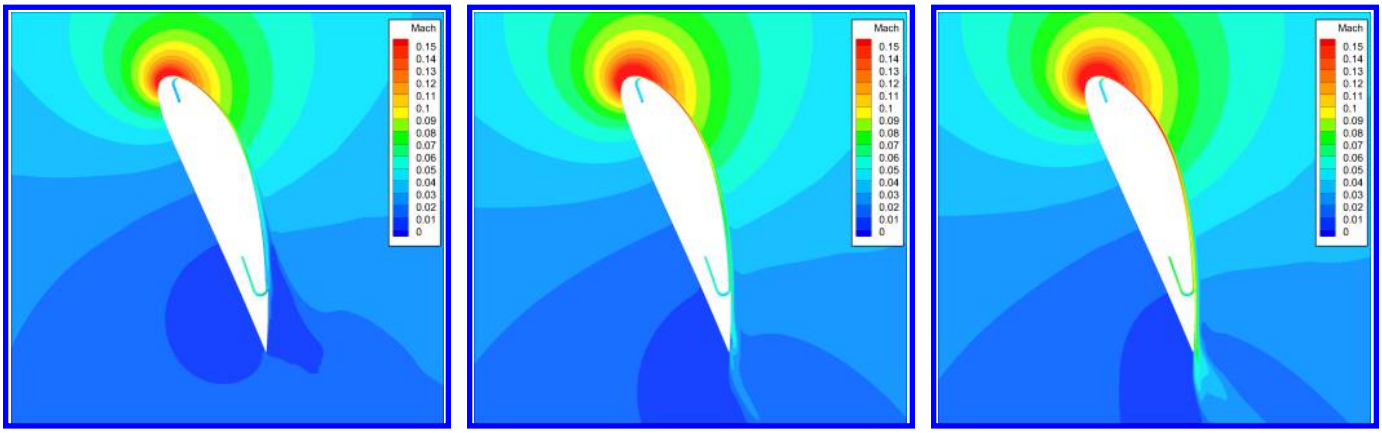


$C_\mu = 0.25$ $C_\mu = 0.35$ $C_\mu = 0.5$

Figure 7: Comparison of time-averaged Mach number distribution for different jet momentum coefficient $C_\mu$.

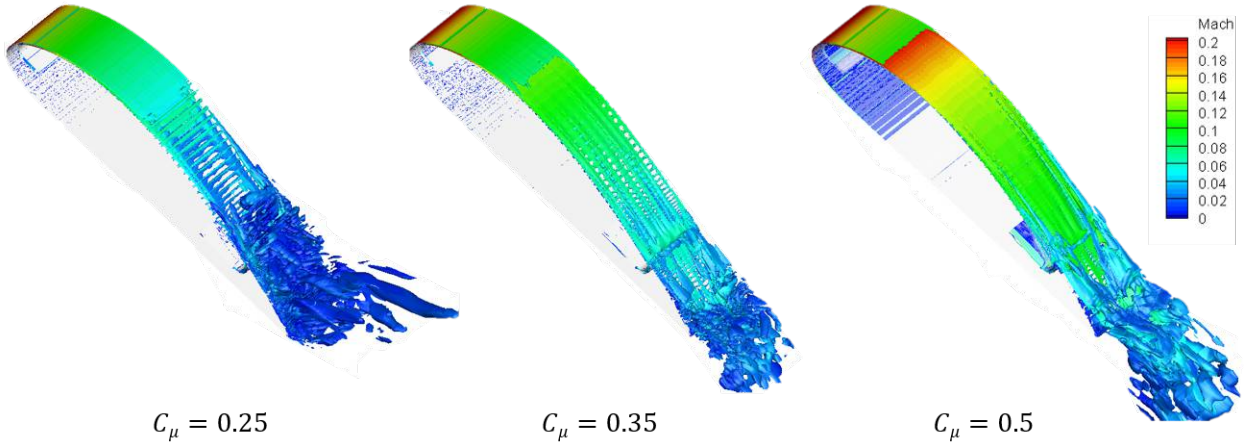


$C_\mu = 0.25$ $C_\mu = 0.35$ $C_\mu = 0.5$

Figure 8: Turbulent flow structures of instantaneous flow field using iso-surface of Lambda-2 criterion colored by Mach number for the CFJ wing with different $C_\mu$.

The instantaneous turbulent flow structures represented by Lambda-2 vortex criterion at $\lambda$ = -100 is shown in Fig. 8. Lambda-2 is a negative second eigenvalue of $S_{ik}S_{kj} + \Omega_{ik}\Omega_{kj}$, in which the strain tensor $S_{ij}$ is defined as $0.5(du_i/dx_j + du_j/dx_i)$ and $\Omega_{ij}$ is the vorticity tensor defined as $0.5(du_i/dx_j - du_j/dx_i)$, respectively. $S_{ij}$ represents the symmetric component of the velocity gradient tensor related to the amount of stretching and folding that derives mixing to occur. $\Omega_{ij}$ represents the antisymmetric component of the velocity gradient tensor, which determines the vorticity motion. Lambda-2 is used to reflect various scales and structure of turbulent flow from a three-dimensional velocity field. This criterion had been employed by researchers for various cases such as in aerodynamics [23].

The turbulent flow field is obviously very chaotic with a large range of resolved scales of large eddies. The flow structures display different flow patterns for different $C_\mu$. The comparison in Fig. 8 highlights the fact that the Lambda-2 vortex criterion clearly depicts the locations where the flow detaches from the surface at the lower $C_\mu$ of 0.25. At higher $C_\mu$ of 0.35 and 0.5, the flow is attached to the surfaces and leaves the trailing edge with shedding vortices. The large shedding vortices are considered the coherent vortical structure, which could provide the thrust and carry the extra jet energy.

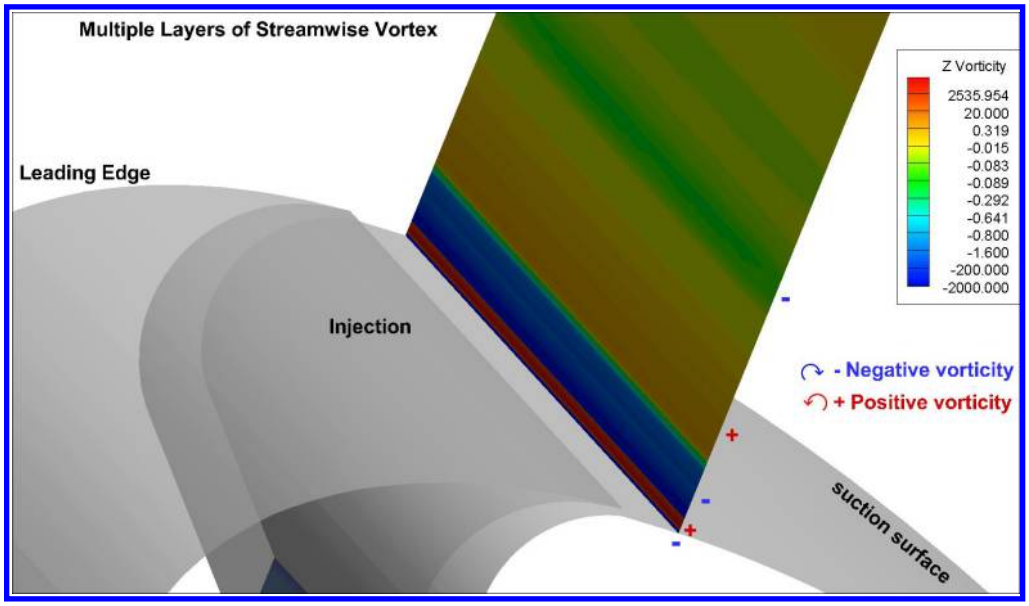


Figure 9: Multiple leading edge vortex layers at $C_\mu$ = 0.5 and AoA = 62°

The vortex layer near the injection is illustrated in Fig. 9, which is similar to the vortex structures observed in the 2D RANS simulation [1]. The near-wall surface region bounded by the non-slip wall boundary generates a clock-wise boundary layer vortex sheet in blue. The high momentum CFJ forms a counter-clockwise vortex layer is generated downstream the CFJ injection slot. Next to the injection jet mixing layer is a clockwise vortex layer (in red), which is induced by the CFJ via the mixing layer, named induced vortex layer. The induced vortex layer further induces a high-speed jet turning around the leading edge, named as secondary induced jet. The high-speed secondary induced jet creates a counter-clockwise vortex layer to transit the velocity radially to the slower freestream velocity. The last vortex layer is hence named the transitional vortex layer. In general, the clockwise vortex layer contributes to lift generation, and the counter clockwise vortex layer contributes thrust generation.

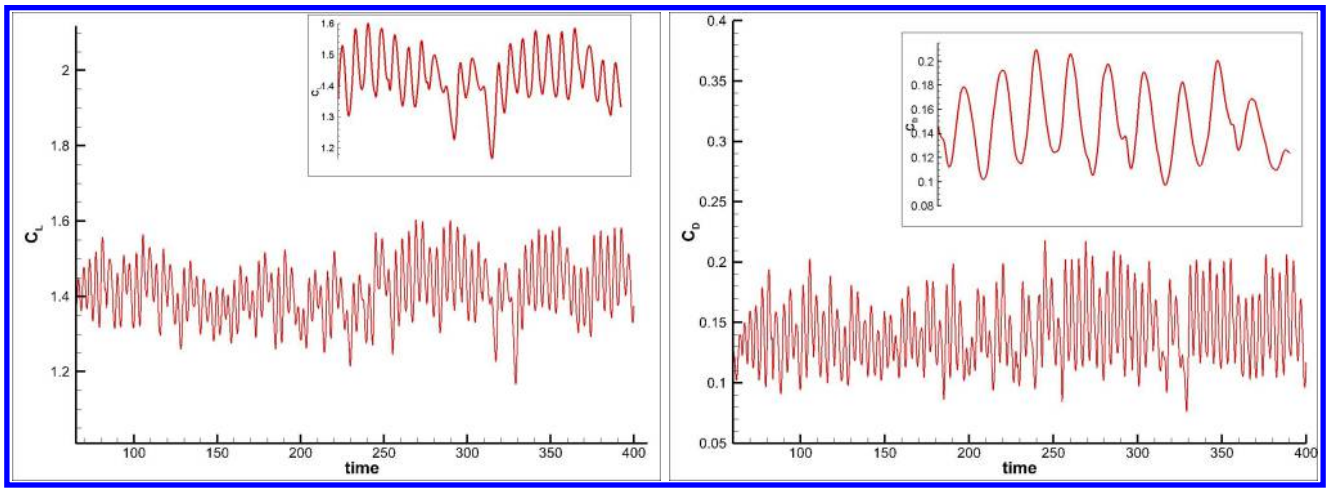


Figure 10: Lift and drag coefficient history for the baseline NACA6421 wing at AoA = 18°

### 5.3 CFJ-NACA6421 and baseline NACA6421 flows at AoA of 18°

As a comparison for reference, the flow of the baseline NACA6421 and CFJ-NACA6421 airfoil is also simulated by IDDES at the AoA = 18°. The lift and drag coefficient history with non-dimensional time is shown in Fig. 10. The time-averaged $C_L$ of IDDES simulation is 1.416 and $C_D$ is 0.149. The simulation results show excellent agreement with the experimental result of $C_L = 1.411$ and $C_D = 0.162$ [24]. The discrepancy of $C_L$ is 0.3%. The IDDES simulation demonstrates its high accuracy against experimental results.

Table 6: Time-averaged simulation results of NACA6421 airfoil

| airfoil | AoA | $C_\mu$ | $C_L$ | $C_D$ |
|---|---|---|---|---|
| NACA6421 Exp.* | 17.5 | - | 1.411 | 0.149 |
| NACA6421 Sim. | 18 | - | 1.416 | 0.162 |
| CFJ6421 Sim. | 18 | 0.25 | 3.8 | -0.12 |

* The experimental data is from NACA TECHNICAL NOTE NO. 392 [24].

Fig. 11 shows the instantaneous Mach number contours and streamlines for the turbulent flow of NACA6421 airfoil at AoA = 18°. It is seen that the boundary layer is at its inception of separation, resulting in a very weak recirculation region. Fig. 11 depicts the instantaneous turbulent flow structures using the Lambda-2 vortex identification criterion. Large vortical flow structure is created by the mildly separated flow from the upper surface. The boundary layer flow detachment takes place where both the pressure and velocity are relatively low.

To compare the CFJ airfoil flow at the same AoA with the same baseline airfoil, The flow structures of for CFJ-NACA6421 wing at AoA = 18° and $C_\mu = 0.25$ are shown in Fig. 13 using the instantaneous Mach number contour and streamlines. The airfoil with CFJ flow control has the flow very well attached with various scale structures near the trailing edge.

## 6 Conclusion

The CFJ flow control airfoil is studied by using IDDES. The three-dimensional flow structures and vortices at high AoAs are investigated. Three different jet momentum coefficient from $C\mu = 0.25$ to $C\mu = 0.5$ simulated at

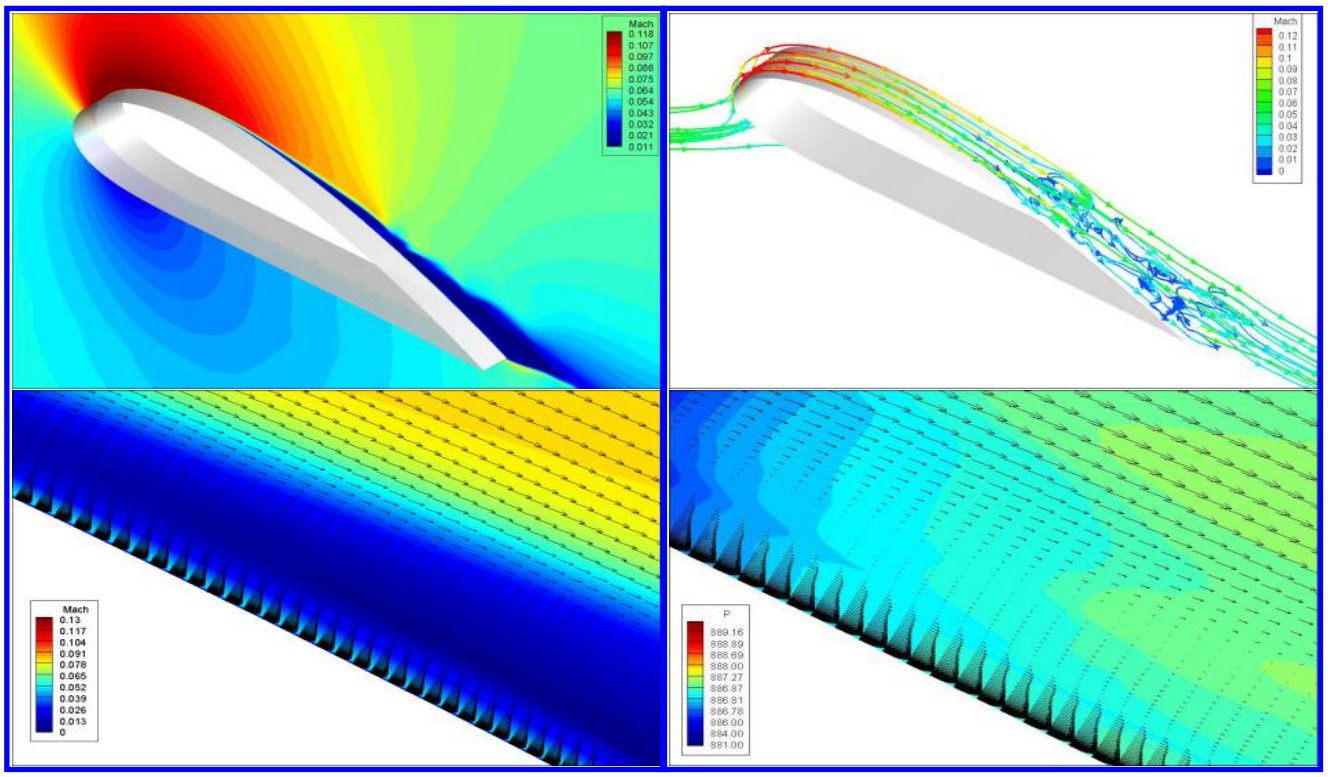


Figure 11: Instantaneous Mach number contour with streamlines and vorticity visualized by the Q=5 criterion for the baseline NACA6421 wing at AoA = 18°

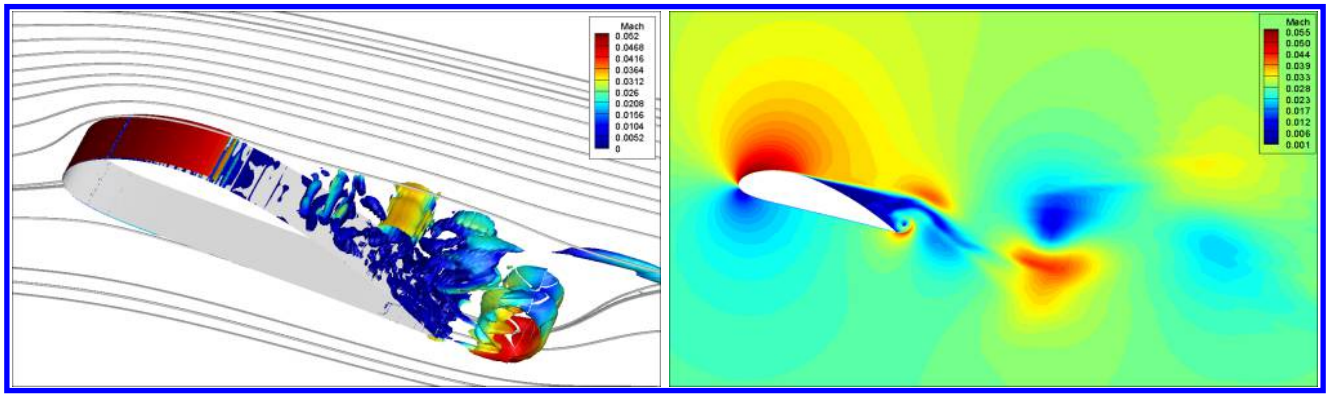


Figure 12: Instantaneous turbulent flow structures represented by Lambda-2 criterion $\lambda_2$=-100 colored by the Mach number

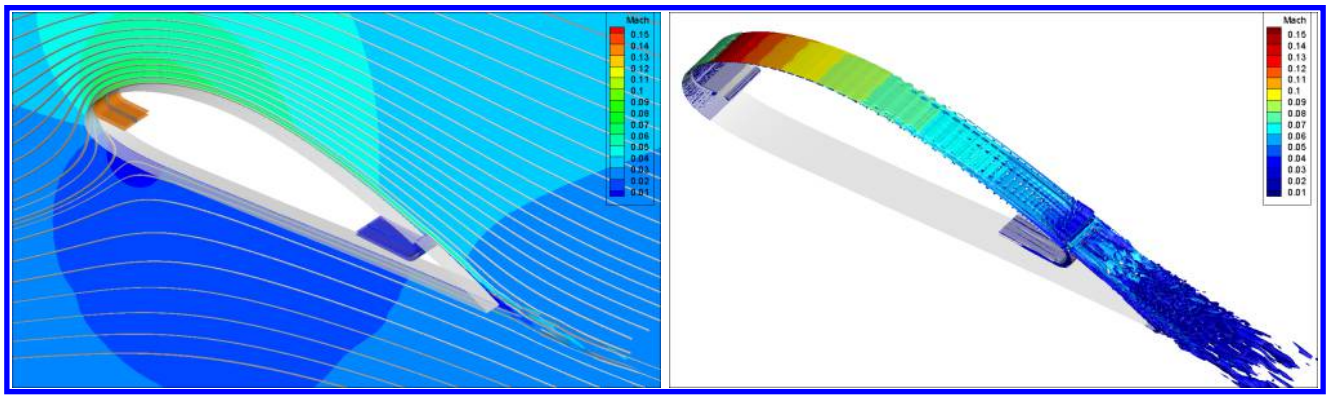


Figure 13: Mach number contour and streamlines for CFJ6421 wing at AoA = 18° and $C_\mu$=0.25



the Mach number of 0.028 and the Reynolds number of $4.8 \times 10^5$. The present numerical study indicates that CFJ active flow control airfoil is able to achieve the super-lift coefficient exceeding the theoretical limit at a very high AoAs with attached flow. The super-lift coefficient is achieved by the three-dimensional IDDES study. The qualitative counter-rotating vortex structures at very high AoA and severe adverse pressure gradient is similar to those observed in 2D RANS simulation.

## 7 Acknowledgment

This project is sponsored by the Defense Advanced Research Projects Agency and monitored by the program manager Jean-Charles Ledé under Cooperative Agreement No.: HR0011-16-2-0052. The content of the information does not necessarily reflect the position or the policy of the Government, and no official endorsement should be inferred. The simulations are conducted on Pegasus supercomputing system at the Center for Computational Sciences at the University of Miami.

# References


[1] Yunchao Yang and Gecheng Zha, "Super-Lift Coefficient of Active Flow Control Airfoil: What is the Limit?." AIAA Paper 2017-1693, AIAA SCITECH2017, 55th AIAA Aerospace Science Meeting, Grapevine, January 9-13 2017.

[2] J. Wimpress, "Aerodynamic technology applied to takeoff and landing," *Annals of the New York Academy of Sciences*, vol. 154, no. 1, pp. 962–981, 1968.

[3] G.-C. Zha, W. Gao, and C. Paxton, "Jet Effects on Co-Flow Jet Airfoil Performance," *AIAA Journal, No. 6,*, vol. 45, pp. 1222–1231, 2007.

[4] G.-C. Zha and D. C. Paxton, "A Novel Flow Control Method for Airfoil Performance Enhancement Using Co-Flow Jet." *Applications of Circulation Control Technologies*, Chapter 10, p. 293-314, Vol. 214, Progress in Astronautics and Aeronautics, AIAA Book Series, Editors: Joslin, R. D. and Jones, G.S., 2006.

[5] G.-C. Zha, C. Paxton, A. Conley, A. Wells, and B. Carroll, "Effect of Injection Slot Size on High Performance Co-Flow Jet Airfoil," *AIAA Journal of Aircraft*, vol. 43, 2006.

[6] G.-C. Zha, B. Carroll, C. Paxton, A. Conley, and A. Wells, "High Performance Airfoil with Co-Flow Jet Flow Control," *AIAA Journal*, vol. 45, 2007.

[7] Wang, B.-Y. and Haddoukessouni, B. and Levy, J. and Zha, G.-C., "Numerical Investigations of Injection Slot Size Effect on the Performance of Co-Flow Jet Airfoil ," *AIAA Journal of Aircraft*, vol. 45, pp. 2084–2091, 2008.

[8] B. P. E. Dano, D. Kirk, and G.-C. Zha, "Experimental Investigation of Jet Mixing Mechanism of Co- Flow Jet Airfoil." AIAA-2010-4421, 5th AIAA Flow Control Conference, Chicago, IL, 28 Jun - 1 Jul 2010.

[9] B. P. E. Dano, G.-C. Zha, and M. Castillo, "Experimental Study of Co-Flow Jet Airfoil Performance Enhancement Using Micro Discreet Jets." AIAA Paper 2011-0941, 49th AIAA Aerospace Sciences Meeting, Orlando, FL, 4-7 January 2011.

[10] Lefebvre, A. and Zha, G.-C. , "Design of High Wing Loading Compact Electric Airplane Utilizing Co-Flow Jet Flow Control." AIAA Paper 2015-0772, AIAA SciTech2015: 53nd Aerospace Sciences Meeting, Kissimmee, FL, 5-9 Jan 2015.

[11] Lefebvre, A. and Dano, B. and Bartow, W. and Di Franzo, M. and Zha, G.-C., "Performance Enhancement and Energy Expenditure of Co-Flow Jet Airfoil with Variation of Mach Number." AIAA Paper 2013-0490, AIAA Journal of Aircraft, DOI: 10.2514/1.C033113, 2016.

[12] Liu, Z.-X. and Zha, G.-C., "Transonic Airfoil Performance Enhancement Using Co-Flow Jet Active Flow Control." AIAA Paper 2016-3066, AIAA Aviation, June 13-17 2016.

[13] Y. Yang and G. Zha, "Simulation of airfoil stall flows using iddes with high order schemes," in *46th AIAA Fluid Dynamics Conference*, p. 3185, 2016.

[14] P. R. Spalart and S. R. Allmaras, "A one-equation turbulence model for aerodynamic flows," in *30th Aerospace Sciences Meeting and Exhibit, Aerospace Sciences Meetings, Reno, NV, USA, AIAA Paper 92-0439*, 1992.

[15] Jameson, A., "Time Dependent Calculations Using Multigrid with Applications to Unsteady Flows Past Airfoils and Wings." AIAA Paper 91-1596, 1991.

[16] Zha, G.C., Shen, Y.Q. and Wang, B.Y., "An improved low diffusion E-CUSP upwind scheme ," *Journal of Computer and Fluids*, vol. 48, pp. 214–220, Sep. 2011.

[17] Edwards, J.R., "A Low-Diffusion Flux-Splitting Scheme for Navier-Stokes Calculations," *Computer & Fluids*, vol. 6, pp. 635–659,doi:10.1016/S0045–7930(97)00014–5, 1997.

[18] Shen, Y.Q., and Zha, G.C., "Improvement of the WENO Scheme Smoothness Estimator," *International Journal for Numerical Methods in Fluids*, vol. 64,, pp. 653–675, DOI:10.1002/fld.2186, 2009.

[19] Shen, Y.Q., Zha, G.C., and Wang, B.Y., "Improvement of Stability and Accuracy of Implicit WENO Scheme," *AIAA Journal*, vol. 47, pp. 331–334, DOI:10.2514/1.37697, 2009.

[20] Shen, Y.Q., and Zha, G.C., "Large Eddy Simulation Using a New Set of Sixth Order Schemes for Compressible Viscous Terms," *Journal of Computational Physics*, vol. 229, pp. 8296–8312, doi:10.1016/j.jcp.2010.07.017, 2010.

[21] Shen, Y.Q., Zha, G.C., and Chen, X., "High Order Conservative Differencing for Viscous Terms and the Application to Vortex-Induced Vibration Flows," *Journal of Computational Physics*, vol. 228(2), pp. 8283–8300, doi:10.1016/j.jcp.2009.08.004, 2009.

[22] Lefebvre, A. and Zha, G.-C., "Trade Study of 3D Co-Flow Jet Wing for Cruise Performance." AIAA Paper 2016-0570, AIAA SCITECH2016, AIAA Aerospace Science Meeting, San Diego, CA, 4-8 January 2016.

[23] J. Jeong and F. Hussain, "On the identification of a vortex," *Journal of fluid mechanics*, vol. 285, pp. 69–94, 1995.

[24] E. N. Jacobs and R. M. Pinkerton, "Tests of naca airfoils in the variable-density wind tunnel series 44 and 64," 1931.